Aqueous synthesis of Z-scheme photocatalyst powders and thin-film photoanodes from earth abundant elements

A. Šutka[a,b,*], M. Vanags[c], U. Joost[b,d], K. Šmits[c], J. Ruža[e], J. Ločs[f], J. Kleperis[c], T. Juhna[g]

[a] *Research Laboratory of Functional Materials Technologies, Faculty of Materials Science and Applied Chemistry, Riga Technical University, Paula Valdena 3/7, 1048 Riga, Latvia*
[b] *Institute of Physics, University of Tartu, W. Ostwaldi Street 1, 50411, Tartu, Estonia*
[c] *Institute of Solid State Physics, University of Latvia, Kengaraga 8, Riga LV-1063, Latvia*
[d] *Surface Science Group, Photonics Laboratory, Tampere University of Technology, PO BOX 692, FI-33101 Tampere, Finland*
[e] *Institute of Technical Physics, Faculty of Materials Science and Applied Chemistry, Riga Technical University, Paula Valdena 3/7, 1048 Riga, Latvia*
[f] *Rudolfs Cimdins Riga Biomaterials Innovations and Development Centre of RTU, Institute of General Chemical Engineering, Faculty of Materials Science and Applied Chemistry, Riga Technical University, Pulka 3, 1007 Riga, Latvia*
[g] *Water Research Laboratory, Faculty of Civil Engineering, Riga Technical University, Ķīpsalas 6A, 1048 Riga, Latvia*

ARTICLE INFO

ABSTRACT

Solid-state narrow band gap semiconductor heterostructures with a Z-scheme charge-transfer mechanism are the most promising photocatalytic systems for water splitting and environmental remediation under visible light. Herein, we construct all-solid Z-scheme photocatalytic systems from earth abundant elements (Ca and Fe) using an aqueous synthesis procedure. A novel Z-scheme two-component $Fe_2O_3/Ca_2Fe_2O_5$ heterostructure is obtained in a straightforward manner by soaking various iron-containing nanoparticles (amorphous and crystalline) with $Ca(NO_3)_2$ and performing short (20 min) thermal treatments at 820 °C. The obtained powder materials show high photocatalytic performances for methylene blue dye degradation under visible light (45 mW/cm^2), exhibiting a rate constant up to 0.015 min^{-1}. The heterostructure exhibits a five-fold higher activity compared to that of pristine hematite. The experiments show that amorphous iron-containing substrate nanoparticles trigger the $Fe_2O_3/Ca_2Fe_2O_5$ heterostructure formation. We extended our study to produce $Fe_2O_3/Ca_2Fe_2O_5$ nanoheterostructure photoanodes via the electrochemical deposition of amorphous iron-containing sediment were used. The visible-light (15 mW/cm^2) photocurrent increases from 183 μA/cm^2 to 306 μA/cm^2 after coupling hematite and $Ca_2Fe_2O_5$. Notably, the powders and photoanodes exhibit distinct charge-transfer mechanisms evidenced by the different stabilities of the heterostructures under different working conditions.

1. Introduction

Visible-light photocatalysis is a green, reagent-free and zero-energy technology for energy harvesting and environmental remediation [1]. Photocatalysis is based on semiconductor oxides absorbing light with incident photon energy matching or exceeding the semiconductor's bandgap [2]. Absorbed photons excite electrons to the conduction band (CB) and leave an electron hole in the valence band (VB), thus creating photogenerated electron-hole pairs. In combination with ambient water, the electron-hole pairs trigger the formation of H_2 and O_2 [3] or reactive oxygen species (ROS) with strong oxidation capacity for the degradation of organic substances [4].

Semiconductor photocatalysis has several disadvantages. First, the most excellent photocatalytic material, TiO_2, does not absorb visible light and can only be excited by ultraviolet radiation [5]. Incorporating dopants, such as nitrogen [6], sulfur [7], carbon [8] or transition metals [9], into TiO_2 can add visible-light activity, but the utilized synthesis methods generally have low yield, high cost, or high ecological impact. Additionally, the resulting photocatalytic activities may be limited [10].

Narrow band gap visible-light-absorbing semiconductors (WO_3, Fe_2O_3, $BiVO_4$, etc.) have been demonstrated as promising candidates for photocatalysis [11–13], but nevertheless most have limited photocatalytic efficiency due to the fast recombination of photogenerated charge carriers. Some narrow band gap photocatalysts, for example, Ag_2O and Cu_2O, are especially active using visible light but are not stable [14,15] and suffer from photocorrosion.

One of the most effective strategies to decrease the overall

---

recombination and to improve the photocatalytic efficiency or stability is to increase the spatial separation of photogenerated charge carriers by coupling semiconductor oxides with metal and/or other semiconductors to form two- or three-component systems [16,17]. In the most common system, two semiconductors are coupled with mismatched band edges, generating a potential slope at the interface, which causes electrons to migrate to the component with the more-positive CB edge and causes holes to transfer to the material with the more-negative VB edge. The main drawback of such a system is a decrease of its (overall) redox potential [18].

The most promising photocatalytic materials are all-solid semiconductor systems with a Z-scheme photogenerated charge-transfer mechanism [19]. Z-scheme systems have been reported for water splitting [20], dye degradation [21] and CO_2 conversion [22]. In Z-scheme systems, semiconductors with mismatched band edges are coupled via ohmic contact to position the CB and VB potentials of one semiconductor more negative than those of the other semiconductor [18]. Ohmic contact in a Z-scheme system triggers the recombination of electrons and electron holes with lower reduction or oxidation potential, thus leaving more reducing electrons and more oxidative holes intact and providing enormously high redox potential for the visible-light-active narrow band gap semiconductor system.

The main obstacles for Z-scheme practical applications are complicated (non-industrializable) multistep synthesis methods, small yields and expensive reagents. Moreover, often Z-scheme photocatalyst synthesis are not green, but photocatalysis technology can be fully considered as green if the green synthesis principles have been followed. Additionally, many involved materials are rare or toxic.

Here, we present a novel Z-scheme semiconductor photocatalyst system based on hematite Fe_2O_3 and brownmillerite $Ca_2Fe_2O_5$ with excellent charge separation (reduced recombination), excellent visible-light harvesting ability and high redox potential. Both Fe_2O_3 and $Ca_2Fe_2O_5$ consist from earth abundant elements and are narrow band gap semiconductors with band gap energy approximately 2 eV. Moreover, hematite is n-type semiconductor, but brownmillerite is p-type semiconductor, thus providing ohmic contact and avoiding additional synthesis steps for depostion of electronic mediators between two semiconductors in Z-scheme. Hematite and brownmillerite also exhibit proper band gap positions as described below. The system was made using an aqueous synthesis to maintain green chemistry principles.

2. Experimental section

2.1. Materials

Iron (iii) nitrate nonahydrate ($Fe(NO_3)_3·9H_2O$, $\geq 98\%$), hexamethylenetetramine (HMTA, $C_6H_{12}N_4$, $\geq 99\%$), calcium nitrate tetrahydrate ($Ca(NO_3)_2·4H_2O$, $\geq 99\%$), sodium hydroxide (NaOH, $\geq 98\%$), MB, $C_{16}H_{18}ClN_3S$, $\geq 95\%$), BQ ($C_6H_4(=O)_2$, certified reference material), TEA (($HOCH_2CH_2)_3N$, $\geq 99\%$), and TBA ($C_4H_{10}O$, anhydrous, $\geq 99.5\%$) were provided by Sigma-Aldrich and were used as received without performing additional purification steps. Deionized water (Milli–Q, electrical resistivity 18.2 MΩ cm) was used for the synthesis and photocatalytic tests.

2.2. Synthesis of the nanoparticle substrates, powdered $Fe_2O_3/Ca_2Fe_2O_5$ nanoheterostructures and photoanodes

2.2.1. Amorphous Fe-containing nanoparticles

To synthesize the amorphous iron-based substrate nanoparticles, 0.1 M iron(iii) nitrate was dissolved in deionized water. The obtained iron nitrate solution was mixed with a 0.5 M HMTA aqueous solution at an equivolumetric ratio at room temperature. Brown sediment immediately formed after mixing the two solutions. After stirring for 5 min, the sediment was collected by centrifugation and was washed with water until the pH value reached 7. The obtained nanoparticle

sediment for the heterostructure synthesis was kept in water without drying.

2.2.2. Goethite (α-FeOOH)

Goethite α-FeOOH nanowires were synthesized by chemical precipitation. In a typical procedure, a 0.1 M iron(iii) nitrate aqueous solution was precipitated at room temperature by the dropwise addition of a 0.5 M NaOH aqueous solution. The obtained sediments were stirred for an additional 30 min and aged for 72 h at 60 °C. The obtained yellow goethite nanowires were collected using centrifugation, washed by water until neutral pH value and stored in water without drying.

2.2.3. Hematite (α-Fe_2O_3)

Crystalline (colloidal) α-Fe_2O_3 nanoparticles (Fe_2O_3 (HU)) were synthesized by hydrothermal synthesis. During the synthesis, 40 ml of a 0.1 M iron(iii) nitrate aqueous solution was poured into a 50 ml Teflon-sealed stainless-steel autoclave and hydrothermally treated at 150 °C for 24 h. As for the other nanoparticle substrates for the heterostructure synthesis, the nanoparticles were washed and stored in water without drying to prevent agglomeration.

2.2.4. $Fe_2O_3/Ca_2Fe_2O_5$ nanoheterostructure

For the synthesis of the $Fe_2O_3/Ca_2Fe_2O_5$ nanoheterostructures, various substrate nanoparticles were dispersed in a $Ca(NO_3)_2$ solution, filtered, dried at 60 °C and heat treated at 820 °C for 20 min in the ambient atmosphere. To control amount of $Ca_2Fe_2O_5$, before filtering and annealing, the substrate nanoparticles were dispersed in 0.1 M, 0.5 M and 1 M aqueous solutions of calcium nitrate.

2.2.5. Fe_2O_3 and $Fe_2O_3/Ca_2Fe_2O_5$ nanoheterostructure photoanodes

The amorphous iron-containing substrate films were prepared by potentiostatic anodic electrodeposition on working electrodes – FTO-coated glass slides (surface resistivity ~7 Ω/sq, Sigma-Aldrich). Electrodeposition was performed from a 0.02 M $FeCl_2$ aqueous solution using a Pt wire as the counter electrode by applying a potential of 1.2 V. The deposition time and annealing temperature were 35 min and 40 °C, respectively. To obtain the $Fe_2O_3/Ca_2Fe_2O_5$ nanoheterostructure photoanode, amorphous iron-containing substrate films were immersed in a $Ca(NO_3)_2$ solution, dried at 60 °C and heat treated at 820 °C for 20 min.

2.3. Structural characterization

The crystalline phases of the synthesized samples were analyzed by powder XRD. A Ultima+ diffractometer (Rigaku, Japan) with Cu-Kα radiation was used for experiments. The SEM morphology studies were performed on a Helios Nanolab, FEI. Electron microscopy at high magnification was performed using TEM (Tecnai G2 F20, FEI) operated at 200 kV. To obtain better phase contrast of the different particles on the nanoheterostructures, STEM was used. EDX was used for sample elemental analysis to verify selected particles on the nanoheterostructures.

The specific surface areas of the synthesized powders were analyzed by recording nitrogen adsorption–desorption isotherms using a NOVA 1200e instrument (Quantachrome, UK). The specific surface areas, S (m^2/g), for the synthesized samples were calculated by the BET method. The surface charges (zeta potentials) of aqueous suspensions of hematite (~0.5 mg/mL) were measured using a Zetasizer Nano ZSP (Malvern Instruments).

The optical absorption spectra of the samples in visible range were measured by a UV-NIR spectrophotometer (Agilent, Cary 4000 UV–vis, Germany). XPS was used to investigate the chemical states and elemental compositions of the heterostructure powders and photoanodes. The powders for XPS measurements were pressed in indium. A surface station equipped with an electron energy analyzer (SCIENTA SES 100) and a non-monochromatic twin anode X-ray tube (Thermo XR3E2) with a characteristic energy of 1253.6 eV (Mg Kα1,2 FWHM 0.68 eV) were
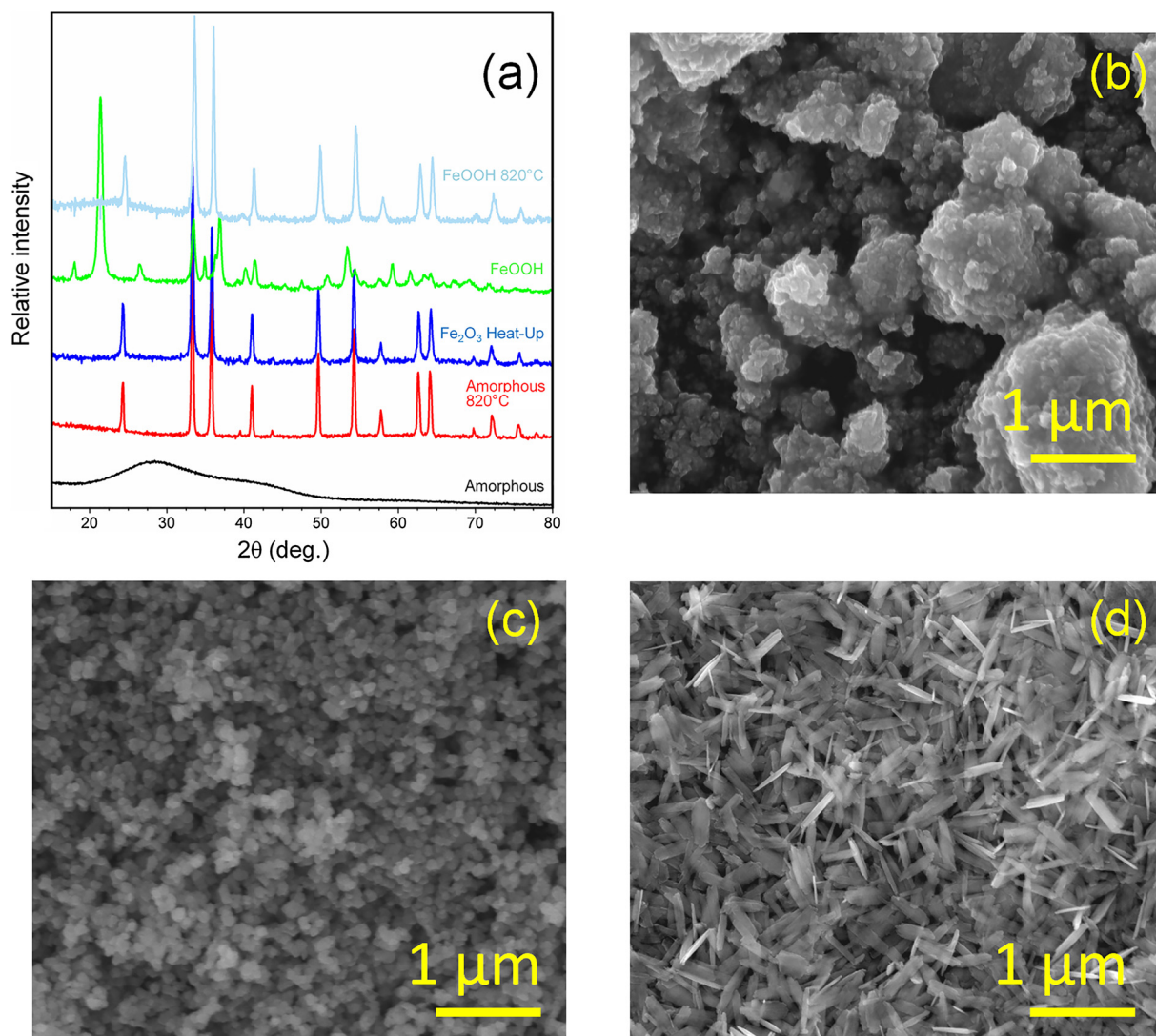
Fig. 1. XRD patterns (a) of different substrate nanoparticles before and after thermal treatment; SEM images of the as-prepared amorphous iron-containing substrate nanoparticles (b), Fe_2O_3 obtained by hydrothermal synthesis (c) and goethite nanowires (d).

used for XPS measurements. Ultra-high vacuum with a base-pressure lower than 8×10^{-10} mbar was used for the XPS measurements. The binding energy was corrected in XPS experiments by using adventitious C1s, C−C peak at 284.8 eV.

2.4. Photocatalytic activity studies

Photocatalytic activities and photocorrosion stabilities of the powder samples were estimated by the photocatalytic degradation of MB dye in aqueous solution (dye concentration 10 mg/l, photocatalyst loading 1 mg/mL) under visible-light irradiation. The light source used for experiments was a 100 W light-emitting diode (LED) (emission band approximately 415–700 nm, i.e., 2.99 eV to 1.77 eV) with an effective power density of 45 ± 3 mW/cm^2. The photocatalytic tests were performed at room temperature in closed 20 ml glass vials. Constant stirring was provided during the tests.

Before the photocatalytic measurements, the powders were dispersed in glass vials using a Hielscher UP50H Compact Lab Homogenizer at maximum intensity for 3 min. The suspensions were kept in the dark until absorption-desorption equilibrium was observed.

The photocatalytic degradation rate of MB was monitored by sampling 1.4 ml from each suspension after a certain time interval. After centrifuging, the supernatant was analyzed by the spectrophotometer.

The photocatalytic activity was estimated by calculating the rate constant (k) of MB degradation from a pseudo-first-order reaction kinetic equation, $-\ln(C/C_0) = kt$, where C_0 and C are the initial absorption peak intensity of MB and the absorption peak intensity of MB in solution after a period of time (t). The rate constants k were divided by the BET surface area.

To estimate the photocorrosion stabilities, after the photocatalytic tests, the powders were separated by centrifugation, dried at 60 °C and re-dispersed again for the next measurement cycle.

2.5. PEC measurements

PEC measurements were measured in a three-electrode cell containing 1 M NaOH electrolyte (pH = 13), a platinum wire counter electrode, a sample film on an FTO/glass substrate as the working electrode (1 cm^2) and SCE as the reference electrode. The open circuit potential was measured after 15 min in the dark. The photocurrent was measured using 5 s light pulses followed by 5 s in the dark with a VoltaLab PGZ 301 potentiostat (Radiometer Analytical) measuring the volt-amperic (I–V) curves (potential was scanned from −200 mV to +500 mV with a rate of 5 mV/s). The photocurrent was calculated as the difference between currents in the dark and in the light for selected potential increments. After each sample, the electrolyte solution was
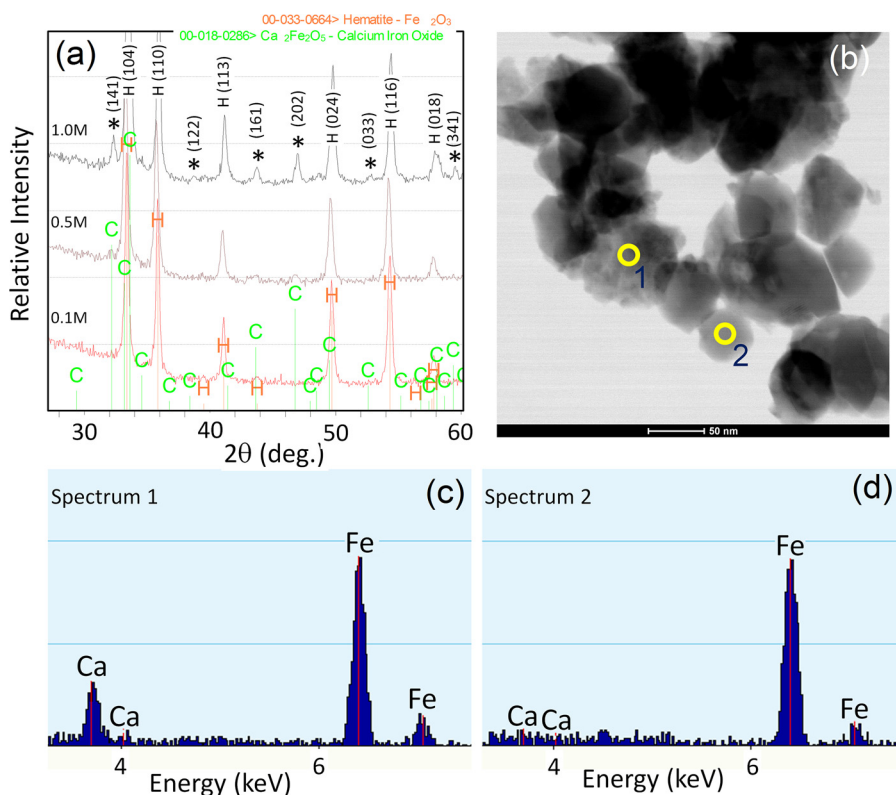
Fig. 2. Left upper panel shows the XRD patterns for the $Fe_2O_3/Ca_2Fe_2O_5$ nanoheterostructures obtained from $Ca(NO_3)_2$ solutions with different molarities. The asterisks on the XRD pattern relate to the brownmillerite phase, while H refers to the hematite phase. Right upper image shows a typical STEM micrograph of the $Fe_2O_3/Ca_2Fe_2O_5$ nanoheterostructure. Selected areas for the EDX analysis are indicated in the STEM micrograph, and the corresponding EDX spectra are shown in the bottom left and right panels.

changed, and the cell was rinsed with deionized water. The light source used for the PEC measurements was a 30 W LED with visible-light irradiation (415–700 nm, 15 ± 1 mW/cm²).

2.6. Mott-Schottky analysis

Fixed frequency (10 kHz) impedance measurements using a VoltaLab PGZ 301 (Radiometer Analytical) impedance analyzer were performed to measure the Mott-Schottky curves. The capacitance was measured for each sample in a frequency of 10 kHz at different biases from −500 mV to 300 mV with a step of 50 mV. The measured capacitance was plotted on a Mott-Schottky graph (1/C2 versus electrode potential) using the equation:

$$\frac{1}{C^2} = \frac{2}{e\varepsilon_0\varepsilon N}\left(V_{app} - V_{FB} - \frac{kT}{e}\right)$$

(1)

where C is the capacitance of the barrier layer, V_{app} is the applied bias potential, V_{FB} is the flat band potential, N is the concentration of donor charge carriers, and T is the absolute temperature. The VFB value was determined by extrapolating the linear region in the Mott-Schottky plot to zero.

3. Results and discussion

3.1. Iron-containing (substrate) nanoparticle formation and structural properties

Various iron-containing substrates were used for the preparation of $Fe_2O_3/Ca_2Fe_2O_5$ nanoheterostructures. Nanosized particle substrates were dispersed in Ca^{2+}-containing aqueous solution, filtered and heat treated. Upon heating, Ca^{2+} reacts with the iron species to form the $Fe_2O_3/Ca_2Fe_2O_5$ nanoheterostructure. A similar strategy was demonstrated by K.J. McDonalds and K.S. Choi, where crystalline α-Fe_2O_3 electrodes were immersed in Zn^{2+}-containing solution and heat treated to obtain $Fe_2O_3/ZnFe_2O_4$ [23]. The tight interface between the semiconductors in the nanoheterostructure enhances charge transfer and the

photocatalytic performances [16,24]. If charge-carrier transfer/mobility is hindered, electron and electron-hole pairs will be more likely to recombine [24]. Here, to achieve effective interfacial charge transfer between Fe_2O_3 and $Ca_2Fe_2O_5$, various iron-containing nanoparticle substrates, such as amorphous precipitates and two crystalline substrates with different surface chemistry (α-Fe_2O_3 nanoparticles and α-FeOOH nanowires), were tested. The formation of $Ca_2Fe_2O_5$ should be easier on amorphous substrate nanoparticles. For crystalline materials, solid-state reactions are limited due to ion diffusion, while amorphous substrate nanoparticles serve as a site for the re-precipitation of a crystalline phase [25].

All the nanoparticle substrate materials were synthesized by environmentally friendly, scalable and straightforward aqueous chemistry methods. Amorphous iron-based substrate nanoparticles were obtained by mixing iron nitrate and hexamethylenetetramine (HMTA) water solutions at room temperature. The addition of the HMTA solution increases the pH of the ferric aqueous solution from 2.01 to 4.87, and consequently, iron nitrate hydrolysis occurs. As confirmed by X-ray diffraction (XRD) measurements (Fig. 1(a)), amorphous precipitates form after mixing the precursors. The use of amorphous nanoparticle substrates is important for the synthesis of the $Fe_2O_3/Ca_2Fe_2O_5$ nanoheterostructure immediately after the procedure (sedimentation and washing by water), as storage in water leads to the formation of iron oxide hydroxide, FeO(OH), crystals, as demonstrated by the XRD pattern in the Electronic Supplementary information (ESI), Fig. S1. Additionally, to obtain amorphous iron-containing nanoparticles, the ferric nitrate and HMTA solutions must be mixed at room temperature. Precipitation at higher temperatures triggers crystallization of α-FeOOH and α-Fe_2O_3. ESI Fig. S2 presents the XRD plot for the sediment obtained upon mixing the ferric nitrate and HMTA solutions in water at 80 °C, where the goethite and hematite phases are clearly distinguished. The microstructure of the sediment was studied by scanning electron microscopy (SEM) (Fig. 1(b), which revealed the formation of densely packed nanoparticle agglomerates with indeterminable particle size; however, the particle diameter is clearly estimated in the nanometer range. The relatively small particle size can be explained by the overall
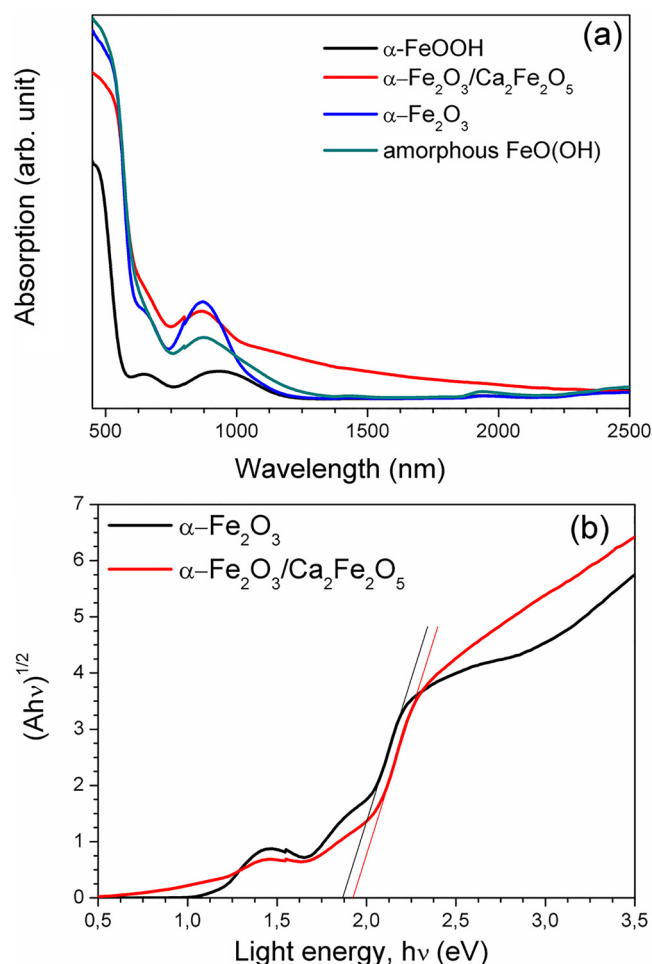
Fig. 3. UV-vis-NIR absorption spectra (Kubleka-Munk function) of various substrate nanoparticles and the $Fe_2O_3/Ca_2Fe_2O_5$ nanoheterostructure (a); optical absorption $(\alpha h\nu)^{1/2}$ versus photon energy plots for α-Fe_2O_3 and the $Fe_2O_3/Ca_2Fe_2O_5$ nanoheterostructure (b).

tendency to obtain smaller sized particles at lower synthesis temperatures. Heat treatment of the amorphous precipitate at 820 °C for 20 min yields the pure hematite α-Fe_2O_3 (A) (ICDD 00-006-0502) nanoparticles, as demonstrated by the XRD pattern in Fig. 1(a), thus demonstrating the potential to use the obtained precipitates to construct the hematite-based $Fe_2O_3/Ca_2Fe_2O_5$ nanoheterostructure.

Crystalline (colloidal) α-Fe_2O_3 (HU) nanoparticles were synthesized by a hydrothermal synthesis approach, where the Fe^{3+} nitrate solution in water was heated at 150 °C for 24 h for homogeneous nucleation, particle growth and α-Fe_2O_3 crystallization [26]. Phase-pure well-crystalline hematite was obtained immediately after the synthesis, as indicated by XRD (Fig. 1(a)), which shows a diffraction pattern with sharp hematite-related peaks (ICDD 00-006-0502) and no adjacent phases. SEM shows hematite particle formation with diameters from 10 nm up to 100 nm during the hydrothermal synthesis, as demonstrated in Fig. 1(c).

Goethite α-FeOOH nanowires were obtained via the precipitation of iron nitrate by NaOH solution in water and aging for 72 h at 60 °C. The precipitation synthesis yielded phase-pure goethite α-FeOOH (ICDD 04-015-2899) with a typical orthorhombic structure, as confirmed by XRD (Fig. 1(a)). The sharp diffraction peaks of the a-FeOOH nanowires indicate a well-crystallized material. No peaks arising from impurities were detected by XRD. The formation of one-dimensional α-FeOOH nanowires was confirmed by SEM (Fig. 1(d)). The synthesized nanowires are up to 500 nm long, and the diameters vary from 20 to 150 nm with an aspect ratio up to 30. Transmission electron microscopy (TEM)

images (ESI, Fig. S3) show that most of the goethite nanowires are grouped in bundles, and the actual diameter of a single nanowire is approximately 21 ± 5.5 nm. The α-FeOOH nanowires form during the precipitation synthesis by the olation of tetrameric polycation species to embryos of octahedral double chains, which is a characteristic of the goethite structure [27]. Goethite nanowires transform to phase-pure hematite α-Fe_2O_3 (NW) upon annealing at 820 °C for 20 min, as demonstrated in Fig. 1(a).

3.2. Formation and structural properties of $Fe_2O_3/Ca_2Fe_2O_5$ nanoheterostructure powders

Briefly, to obtain the $Fe_2O_3/Ca_2Fe_2O_5$ nanoheterostructure, substrate nanoparticles were dispersed in $Ca(NO_3)_2$ solution, filtered, dried and thermally treated at 820 °C for 20 min in the ambient atmosphere. The amount of $Ca_2Fe_2O_5$ can be controlled by molarity of $Ca(NO_3)_2$. Phases on the XRD pattern (Fig. 2(a) and ESI, Fig. S4) related to hematite (ICDD 00-033-0664) and brownmillerite $Ca_2Fe_2O_5$ (ICDD 04-002-2559) were observed using the amorphous nanoparticle substrates. Increased peak intensities related to the $Ca_2Fe_2O_5$ phase were observed upon increasing the molarity of the $Ca(NO_3)_2$ solution. The observed XRD pattern is in well accordance with the results from scanning transmission electron microscopy (STEM) and energy dispersive X-ray (EDX) spectroscopy analysis on single nanocrystals (Fig. 2(b–d)), which revealed the presence of both calcium and iron within the nanocrystal heterodimers, while only iron was observed on the hematite particle. The XRD peaks related to the $Ca_2Fe_2O_5$ phase are not as strongly observed after the heat treatment of the $Ca(NO_3)_2$-soaked colloidal α-Fe_2O_3 nanoparticles and goethite α-FeOOH substrates (ESI, Fig. S5). Additionally, the presence of Ca^{2+} in the $Ca(NO_3)_2$-soaked and thermally treated α-FeOOH is confirmed by the EDX studies presented in ESI, Fig. S6. Moreover, the Ca quantities in the heterostructures derived from the α-FeOOH and amorphous iron-containing nanoparticles are very similar (~5 wt%). The amorphous iron-containing nanoparticle substrates could provide more surface sites and open pores and a higher surface area for precursor spatial infiltration and adsorption with a higher abundancy of Fe cations for $Ca_2Fe_2O_5$ formation upon heat treatment. The surface of the goethite crystals presents a highly dense coating of $-OH$ groups, and heating transforms goethite to Fe_2O_3 by releasing water based on the reaction: $2FeOOH \rightarrow Fe_2O_3 + H_2O$. Water release during the phase transition may prohibit Fe supply for $Ca_2Fe_2O_5$ formation. The goethite wires also exhibit the lowest surface area among the substrate nanoparticles used for the $Fe_2O_3/Ca_2Fe_2O_5$ nanoheterostructure synthesis. The multipoint Brunauer-Emmett-Teller (BET) specific surface area values for amorphous iron-containing substrates, crystalline α-Fe_2O_3 and α-FeOOH were 115.7 m^2/g, 109.40 m^2/g and 60.23 m^2/g, respectively.

3.3. Optical properties of the substrate nanoparticles and $Fe_2O_3/Ca_2Fe_2O_5$ nanoheterostructure powders

Fig. 3 shows the UV–vis absorption spectra (Kubelka-Munk function) of the FeO(OH), α-Fe_2O_3 and α-FeOOH substrate nanoparticles and the $Fe_2O_3/Ca_2Fe_2O_5$ nanoheterostructure. All the materials exhibit (poorly defined) absorption bands centered at 650 nm and broad absorption bands in the wavelength range of 700–1000 nm, which correspond to the $^6A_1(^6S) \rightarrow {}^4T_2(^4G)$ and $^6A_1(^6S) \rightarrow {}^4T_1(^4G)$ ligand-field transitions of Fe^{3+}, respectively [28]. The optical band gaps for hematite (1.86 eV) and for the $Ca_2Fe_2O_5/Fe_2O_3$ nanoheterostructure (1.92 eV) were observed from the optical absorption $(\alpha h\nu)^{1/2}$ versus photon energy plots by extrapolating linear fits of the plots to zero [29]. The band gap values for hematite are usually dependent on the synthesis method and have been reported to be between 1.9 to 2.2 eV [30]. The observed blueshift for the heterostructure in comparison with hematite is related to the higher band gap (2.2 eV) of pristine $Ca_2Fe_2O_5$ [31].
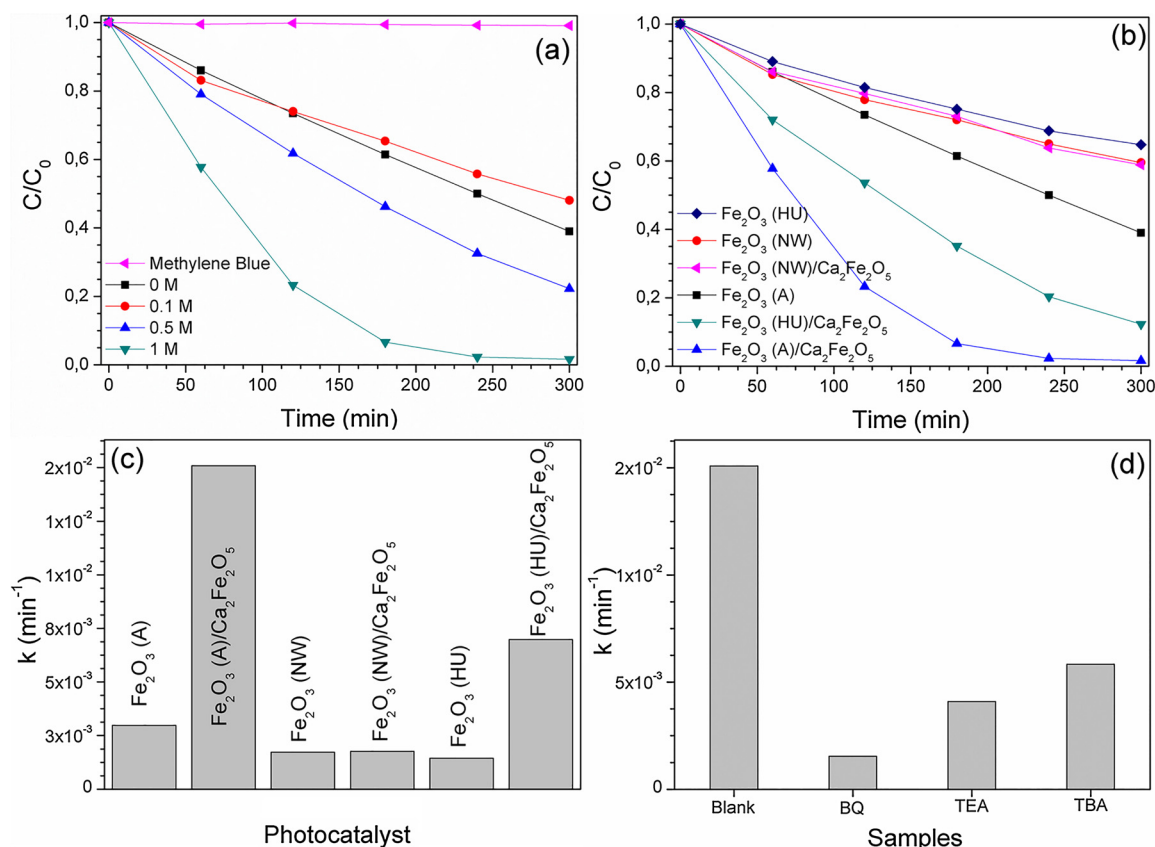
Fig. 4. The photocatalytic properties of the synthesized materials. (a) MB photocatalytic degradation in water (10 mg/l) under visible light by the $Fe_2O_3/Ca_2Fe_2O_5$ nanoheterostructures obtained from amorphous substrate nanoparticles soaked in $Ca(NO_3)_2$ solutions with different molarities. (b) MB photocatalytic degradation by various $Fe_2O_3/Ca_2Fe_2O_5$ nanoheterostructures obtained from the $Ca(NO_3)_2$ solution using different substrate nanoparticles (Fe_2O_3 (A) – amorphous iron-containing sediment, Fe_2O_3 (HU) – hematite obtained from hydrothermal synthesis and Fe_2O_3 (NW) – FeOOH nanowires. (c) Pseudo-first-order rate constants (k) for the different $Fe_2O_3/Ca_2Fe_2O_5$ nanoheterostructures. (d) Effects of a series of chemical scavengers on the MB degradation k: BQ (0.1 mmol/L) for scavenging $\cdot O^{2-}$, TEA (1 mmol/L) for quenching h^+, and TBA (1 mmol/L) for scavenging $\cdot OH$ on Fe_2O_3 (A)/$Ca_2Fe_2O_5$.

3.4. Photocatalytic dye degradation by hematite and Fe2O3/Ca2Fe2O5 nanoheterostructure powders

The photocatalytic activities of the synthesized materials were estimated by the degradation of methylene blue (MB) under visible-light irradiation ($45 \pm 3 \, mW/cm^2$). The change of the most intense absorption peak of MB centered at 665 nm was evaluated to study MB degradation. The blank experiments show that only a 1% decrease of MB occurs in the absence of a photocatalyst during a 5 h irradiation. α-Fe_2O_3 was obtained by thermal phase transition/treatment at 820 °C for 20 min from: (i) amorphous Fe-containing precipitates (α-Fe_2O_3 (A)), (ii) α-FeOOH nanowires (α-Fe_2O_3 (NW)) and (iii) hydrothermal synthesis derived α-Fe_2O_3 (α-Fe_2O_3 (HU)). The photocatalytic activities of α-Fe_2O_3 were studied to estimate the enhancement in performance after coupling with $Ca_2Fe_2O_5$ (Fig. 4). The pseudo-first-order rate constants (k) for MB degradation for the various hematite samples are very similar and decrease in the following order: α-Fe_2O_3 (A) ($2.97 \cdot 10^{-3} \, min^{-1}$) → α-$Fe_2O_3$ (NW) ($1.73 \cdot 10^{-3} \, min^{-1}$) → α-$Fe2O3$ (HU) ($1.45 \cdot 10^{-3} \, min^{-1}$). The observed rate constants are almost the same as those previously reported for MB degradation under visible-light irradiation by flower-like hierarchical nanosized α-Fe_2O_3 [32].

Multipoint BET surface area measurements revealed the following specific surface area values of the hematite samples: α-Fe_2O_3 (A) ($2.16 \, m^2/g$), α-Fe_2O_3 (NW) ($28.84 \, m^2/g$) and α-Fe_2O_3 (HU) ($12.55 \, m^2/g$). To exclude the effect of the specific surface area, the k values were divided by the surface areas. The specific rate constants for the various samples decrease in the following order: α-Fe_2O_3 (A) ($1.38 \cdot 10^{-3} \, min^{-1} \, g \, m^{-2}$) → α-$Fe_2O_3$ (HU) ($0.11 \cdot 10^{-3} \, min^{-1} \, g \, m^{-2}$) →

Fe_2O_3 (NW) ($0.08 \cdot 10^{-3} \, min^{-1} \, g \, m^{-2}$). The results show that α-Fe_2O_3 (A) exhibits considerably higher photocatalytic activity, which is related to various surface properties. The measured Z-potential values for the various annealed samples were: α-Fe_2O_3 (A) ($+23.9 \, eV$) → α-Fe_2O_3 (HU) ($+17.6 \, eV$) → Fe_2O_3 (NW) ($-37.9 \, eV$).

The k value increased 5.1 times for α-Fe_2O_3 (A) (k = 0.015 min^{-1}) and 4.8 times for α-Fe_2O_3 (HU) (k = 0.007 min^{-1}) when the samples (before thermal treatment) were soaked in 1 M aqueous $Ca(NO_3)_2$ solution. No enhancement was observed for the materials obtained from the α-FeOOH substrate nanoparticles. The samples obtained from the amorphous substrate nanoparticles exhibited two-fold higher rate constants compared to the other samples. We also studied the specific surface areas to normalize the rate constants and exclude the effect of a larger surface area. The specific surface areas were $12.4 \, m^2/g$ and $6.3 \, m^2/g$ for $Fe_2O_3/Ca_2Fe_2O_5$ obtained from α-Fe_2O_3 (A) and α-Fe_2O_3 (HU), respectively. The specific rate constant for $Fe_2O_3/Ca_2Fe_2O_5$ obtained from α-Fe_2O_3 (A) ($1.21 \cdot 10^{-3} \, min^{-1} \, g \, m^{-2}$) is still higher than those observed for the other samples but is similar to the sample obtained from crystalline α-Fe_2O_3 ($1.12 \cdot 10^{-3} \, min^{-1} \, g \, m^{-2}$). The results show that both amorphous iron-containing nanoparticles can be used for substrate materials to obtain an efficient $Fe_2O_3/Ca_2Fe_2O_5$ photocatalyst nanoheterostructure. The sample obtained from the α-FeOOH substrate nanoparticles showed a considerably lower rate constant ($0.034 \cdot 10^{-3} \, min^{-1} \, g \, m^{-2}$), which could be attributed to hindered $Ca_2Fe_2O_5$ formation, as discussed in the section above about the formation and structural properties of the $Fe_2O_3/Ca_2Fe_2O_5$ nanoheterostructure powders.

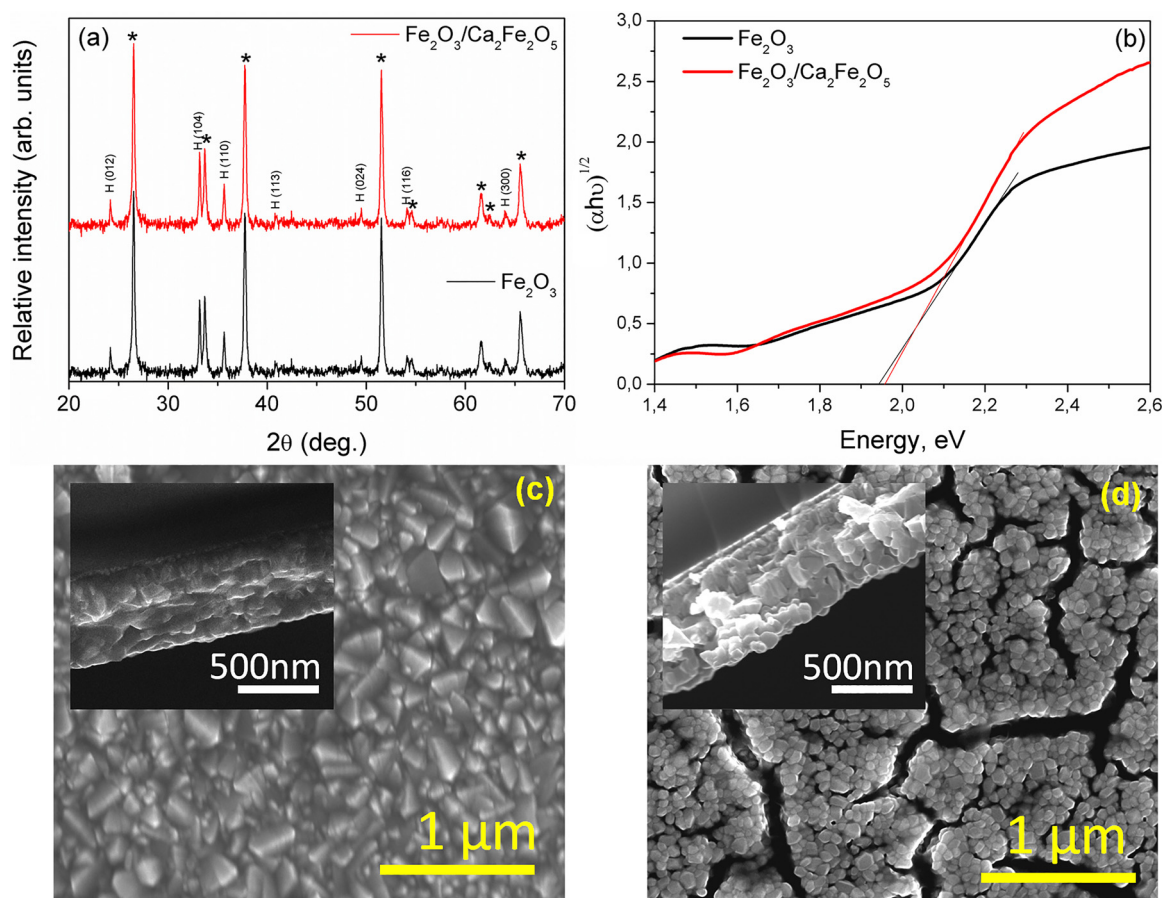The enhanced photocatalytic performance can be attributed to the

Fig. 5. X-ray patterns (a) and optical absorption $(\alpha h \nu)2$ versus photon energy plots (b) of the Fe_2O_3 and $Fe_2O_3/Ca_2Fe_2O_5$ nanoheterostructure photoanodes. The H and asterisk on the XRD patterns relate to hematite and the FTO substrate, respectively. SEM images of (c) Fe_2O_3 and (d) $Fe_2O_3/Ca_2Fe_2O_5$. Insets on the SEM images show the cross-sections of the same samples.

tight interface $Fe_2O_3/Ca_2Fe_2O_5$ nanoheterostructure formation and improved photogenerated charge-carrier separation over the interface. $Ca_2Fe_2O_5$ is a narrow band gap p-type semiconductor with a more-negative CB potential and more-negative VB potential in comparison to hematite [33]. Thus, charge transfer between n-type α-Fe_2O_3 and p-type $Ca_2Fe_2O_5$ can be potentially incorporated into a Z-scheme mechanism, where photoinduced electrons on hematite would recombine with photogenerated electron holes on $Ca_2Fe_2O_5$, leaving electrons on $Ca_2Fe_2O_5$ and electron holes on α-Fe_2O_3 for reduction and oxidation reactions, respectively, and consequently providing a high redox potential for the overall system. Z-scheme photocatalytic systems have been considered the most effective photocatalytic systems due to their excellent charge separation (reduced recombination) and high redox potentials compared to classical heterojunction-type photocatalytic systems, where electrons are transferred to the CB with a lower reducing potential, and electron holes are transferred to the VB with a lower oxidation potential [18]. In a Z-scheme, two semiconductor compounds are primarily coupled via ohmic contact (conductor) with low contact resistance [34]. The first reported all-solid Z-scheme was the three-component semiconductor-conductor-semiconductor system (TiO$_2$-Au-CdS) published in 2006 by Tada et al. [35]. Other two-component solid-state Z-scheme systems, where low contact resistance was provided by conductive contact interface [18] or a p-n junction [36,37], have also been reported. Here, our Z-scheme may be formed through a *p-n* junction between p-type $Ca_2Fe_2O_5$ and n-type α-Fe_2O_3. P-type conductivity in brownmillerite $Ca_2Fe_2O_5$ is provided by oxygen interstitials, which are charge compensated by holes associated with Fe cations due to variable oxidation states [38].

To verify the Z-scheme charge-transfer mechanism, various

scavengers were added during the photocatalytic MB degradation tests. First, benzoquinone (BQ) was added to scavenge superoxide anions, $\cdot O^{2-}$. The k value for MB degradation by Fe_2O_3 (A)/$Ca_2Fe_2O_5$ decreased by an order of magnitude from 0.015 (min^{-1}) to 0.0015 (min^{-1}), indicating that $\cdot O^{2-}$ has a considerable role in MB degradation. However, we did not observe a decrease in photocatalytic activity for bare Fe_2O_3 after BQ addition. The potential for oxygen reduction from O_2 to $\cdot O^{2-}$ is -0.33 eV vs the normal hydrogen electrode (NHE), thus $\cdot O^{2-}$ cannot be generated by photoinduced electrons on the CB of hematite, which has a reduction potential of $+0.2$ eV vs NHE [39], while the CB of $Ca_2Fe_2O_5$ has a more-negative reduction potential than that of oxygen reduction to produce $\cdot O^{2-}$. Therefore, $\cdot O^{2-}$ release was experimentally observed [33]. We also studied the influence of triethanolamine (TEA) to quench holes and tert-butyl alcohol (TBA) for scavenging hydroxyl radicals, $\cdot OH$. Both scavengers displayed an almost equal effect on MB degradation by the photocatalytic process. The rate constants for MB degradation over Fe_2O_3 (A)/$Ca_2Fe_2O_5$ decreased from 0.015 to 0.004 and 0.006 (min^{-1}) with added TEA and TBA, respectively. The VB oxidation potential of α-Fe_2O_3 is sufficiently positive to oxidize H_2O to $\cdot OH$ and H^+ ($H_2O + h^+ \rightarrow \cdot OH + H^+$), where released H^+ can generate ROS H_2O_2 and $\cdot OH$.

3.5. Fe_2O_3 and $Fe_2O_3/Ca_2Fe_2O_5$ photoanodes and their PEC performances

Photoelectrochemical (PEC) measurements were performed on the α-Fe_2O_3 and $Fe_2O_3/Ca_2Fe_2O_5$ photoanodes to gain better understanding of the photoinduced charge-carrier separation and transport over the nanoheterostructure. The photoanodes were obtained in a similar way as the Z-scheme $Fe_2O_3/Ca_2Fe_2O_5$ nanoheterostructure powders – by
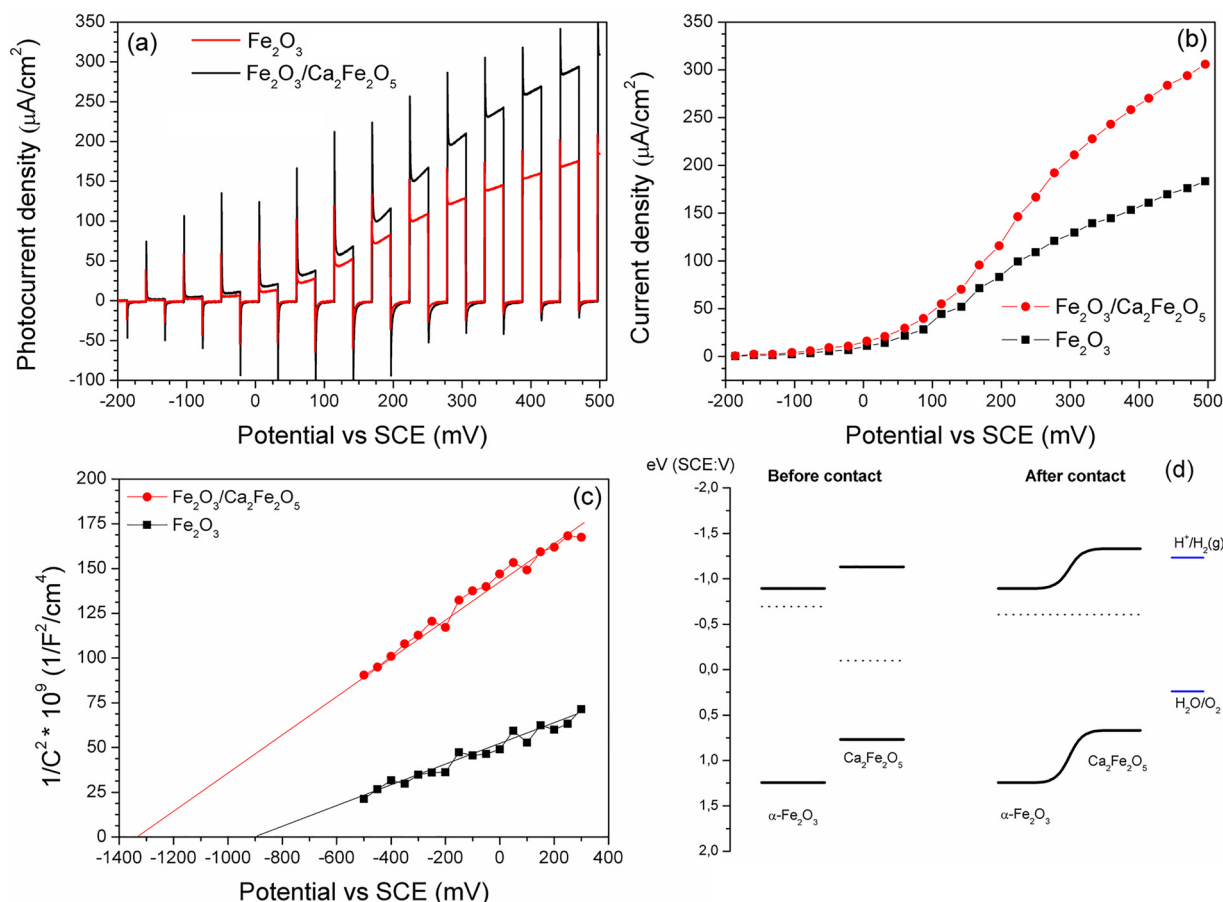
Fig. 6. (a) Photoelectrochemical performance under chopped light illumination, (b) current density vs potential (J-V curves) for the same photoanodes and (c) Mott-Schottky plots of hematite and hematite/brownmillerite photoanodes. (d) Schematic presentation the electronic energy levels before and after the *p-n* heterojunction formation between $Ca_2Fe_2O_5$ and α-Fe_2O_3.

soaking iron-containing sediment in a $Ca(NO_3)_2$ solution and subsequently drying and heating at 820 °C for 20 min. Iron-containing substrate films were prepared by potentiostatic anodic electrodeposition on F-doped SnO_2 (FTO) transparent conductive oxide substrates. The utilized anodic deposition conditions favor the oxidation of Fe^{2+} to Fe^{3+} and precipitation of the amorphous oxyhydroxide [40]. To obtain the Fe_2O_3/$Ca_2Fe_2O_5$ nanoheterostructure, iron-containing substrate films were immersed in a $Ca(NO_3)_2$ solution, dried and heat treated.

The XRD patterns, UV–vis absorption spectra and SEM images of the Fe_2O_3 and Fe_2O_3/$Ca_2Fe_2O_5$ photoanodes are displayed in Fig. 5. The XRD patterns confirm the formation of the hematite phase. The optical band gaps of the obtained Fe_2O_3 and Fe_2O_3/$Ca_2Fe_2O_5$ photoanodes were 1.94 eV and 1.96 eV, respectively. Similar to the powders (see Section 3.3.), a small blue shift was observed upon adding $Ca_2Fe_2O_5$ to Fe_2O_3.

The SEM images show very different morphologies for Fe_2O_3 and the Fe_2O_3/$Ca_2Fe_2O_5$ heterostructure. The hematite photoanode formed from tetragonal-like single crystals with edges up to 500 nm. The heterostructure photoanode reveals a microstructure composed of relatively small (70–150 nm) irregularly shaped nanocrystals and cracks. The cross-sections of both films reveal very similar thicknesses of approximately 850 nm and, again, different morphologies along the entire cross-sections, indicating that calcium nitrate was impregnated deep in the electrochemically deposited iron-containing amorphous substrate layer. The presence of $Ca_2Fe_2O_5$ in the films was confirmed by X-ray photoelectron spectroscopy (XPS) (ESI, Fig. S7). The locations and shapes of the photolines for the Fe_2O_3/$Ca_2Fe_2O_5$ heterostructure powder coincide well with those obtained for previously reported brownmillerite $Ca_2Fe_2O_5$ [31,41]. The Ca 2p3/2 photo line is located at

346.6 eV, and the Fe 2p3/2 maximum is located at 710.5 eV, with a satellite signal associated with Fe^{3+} also present at higher binding energies.

The PEC measurements were measured under visible light (15 ± 1 mW/cm²) in a three-electrode cell containing 1 M NaOH electrolyte (pH = 13), a platinum wire counter electrode, the sample film on an FTO/glass substrate as the working electrode and a saturated calomel electrode (SCE) as the reference electrode. J-V curves for the hematite Fe_2O_3 and Fe_2O_3/$Ca_2Fe_2O_5$ photoanodes are demonstrated in Fig. 6(b). A photocurrent of 183 µA/cm² was observed at 0.5 V for bare hematite, and this photocurrent increased to 306 µA/cm² for Fe_2O_3/$Ca_2Fe_2O_5$. The photocurrent indicates the number of photogenerated holes that reach the semiconductor/liquid interface. The higher photocurrent can be due to the increased relative volume of the space charge layer and enhanced photogenerated charge-carrier separation. Nanostructuring is an effective strategy to increase the relative volume of the space charge layer [42], while heterostructuring enhances charge-carrier separation [16,17]. Our electron microscopy observations reveal a remarkable decrease in grain size for the samples immersed in calcium nitrate before annealing, while charge-carrier separation is improved in the heterostructure because both the CB and VB edges of hematite lie energetically lower than the CB and VB of brownmillerite. Thus, photoinduced electrons are transferred from $Ca_2Fe_2O_5$ to Fe_2O_3 under applied bias and anodic conditions. Moreover, photogenerated electron holes are expected to be transferred from hematite to brownmillerite for oxidation reactions.

The observed results correlate with the Mott-Schottky analysis based on electrochemical impedance measurements in the dark on bare Fe_2O_3 and Fe_2O_3/$Ca_2Fe_2O_5$. The flat band potential (V_{FB}) position was

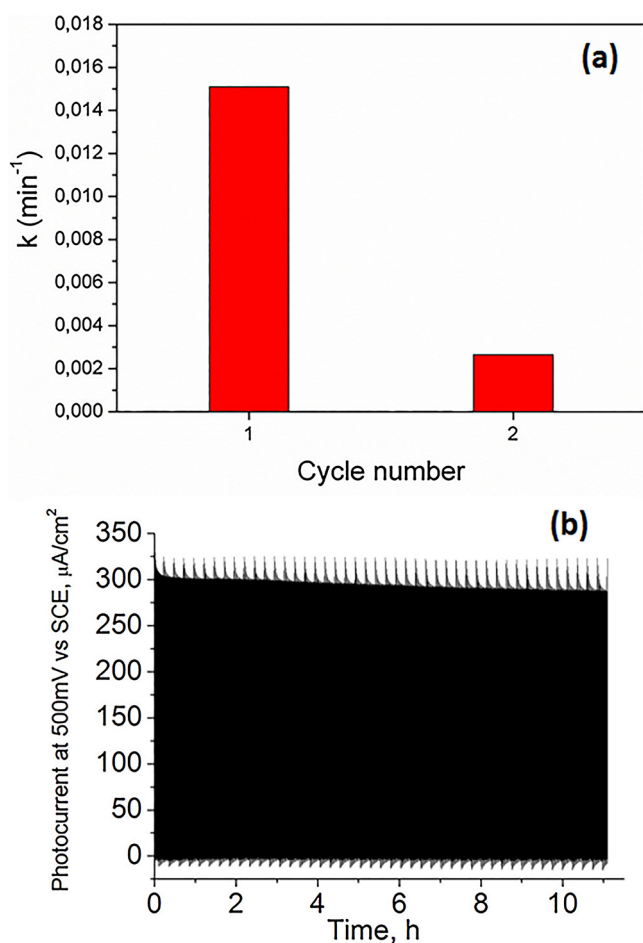**Fig. 7.** (a) Graph showing the decrease of the MB photocatalytic degradation rate constant of the $Fe_2O_3/Ca_2Fe_2O_5$ system under the Z-scheme regime (duration of the first cycle was 1 h). (b) Graph showing the good stability of the $Fe_2O_3/Ca_2Fe_2O_5$ system during PEC measurements.

estimated from the capacitance at the interface between the semi-conductor and electrolyte by extrapolating the $1/C^2$ versus V plot. The observed VFB value was -895 mV versus SCE at pH = 13 for hematite, which is similar to those reported by others for hematite on FTO [43,44]. The VFB increases to -1330 mV when Fe_2O_3 is coupled with $Ca_2Fe_2O_5$, confirming the previously suggested band alignment, which is schematically illustrated in Fig. 6(d).

3.6. Stability of the $Fe_2O_3/Ca_2Fe_2O_5$ heterojunction powders and photoanodes

Finally, the photocatalytic stability of the $Fe_2O_3/Ca_2Fe_2O_5$ system was tested under a Z-scheme regime (powder suspension in MB water solution) as well as using PEC measurements. From cyclic photo-catalytic MB degradation measurements under a Z-scheme regime, we observed a five-fold rate constant decrease already at the second cycle after irradiating for only 3 h in the first cycle (Fig. 7(a)), while the PEC measurements showed very stable behavior with no loss of the measured photocurrent over 12 h of visible-light irradiation (Fig. 7(b)). The observed behavior could be related to the low stability of $Ca_2Fe_2O_5$ against photoreduction. In the Z-scheme regime, photogenerated electrons are separated on the $Ca_2Fe_2O_5$ side, thus triggering its corrosion by photoreduction. XRD of the $Fe_2O_3/Ca_2Fe_2O_5$ powder after three photocatalytic MB degradation cycles shows the formation CaO and $CaFe_2O_4$ impurity phases, indicating that photogenerated occurs via the reaction $Ca_2Fe_2O_5 \rightarrow CaFe_2O_4 + CaO$ (ESI, Fig. S8). Carbonate formation was not observed by XRD, showing that the photocorrosion

mechanism of $Ca_2Fe_2O_5$ in the Z-scheme regime is different from that of bare brownmillerite, which transforms to carbonates during the pho-todegradation process of methylene orange [45].

However, the $Fe_2O_3/Ca_2Fe_2O_5$ system is stable under PEC measurements, indicating a different charge-transfer mechanism. A similar *p-n* junction photoanode, where hematite was coupled with $CaFe_2O_4$, was demonstrated by M.G. Ahmed et al. [44]. Under illumination, photogenerated holes were transferred to $CaFe_2O_4$, while photo-generated electrons transferred from the $CaFe_2O_4$ CB to the Fe_2O_3 CB and further to the contact electrode. Here, under the proposed me-chanism, $Ca_2Fe_2O_5$ in the $Fe_2O_3/Ca_2Fe_2O_5$ system is protected from photocorrosion and thus exhibits stable photocurrent, as demonstrated in Fig. 7(b).

4. Conclusions

An all-solid-state Z-scheme nanoheterostructure was successfully constructed from an earth abundant, environmentally friendly element based on n- and p-type narrow band gap semiconductors, hematite α-Fe_2O_3 and brownmillerite $Ca_2Fe_2O_5$, by soaking Fe-containing nano-particle substrates (free standing particles in suspensions or thin films) with Ca^{2+} aqueous solutions. The heterostructure formation was more pronounced on amorphous Fe nanoparticle substrates than on crystal-line hematite, while the formation of $Ca_2Fe_2O_5$ was not observed on goethite α-FeOOH. In comparison with hematite, the $Fe_2O_3/Ca_2Fe_2O_5$ nanoheterostructure exhibited a five-fold higher photocatalytic dye degradation rate and two-fold enhanced photocurrent. The Z-scheme photoinduced charge-carrier transfer mechanism in the $Fe_2O_3/Ca_2Fe_2O_5$ powders was confirmed by chemical methods, where the photocatalytic activity was strongly influenced by $\cdot O^{2-}$ scavengers. However, the degradation ability of Fe_2O_3 was not influenced by these scavengers. Long-term photocurrent measurements revealed the stable performance of $Fe_2O_3/Ca_2Fe_2O_5$, while $Ca_2Fe_2O_5$ was less stable under the Z-scheme regime due to a lower tolerance against photoreduction.

Appendix A. Supplementary data

Supplementary data associated with this article can be found, in the online version, at https://doi.org/10.1016/j.jece.2018.04.003.

References

[1] S. Dong, J. Feng, M. Fan, Y. Pi, L. Hu, X. Han, M. Liu, J. Sun, J. Sun, Recent de-velopments in heterogeneous photocatalytic water treatment using visible light-responsive photocatalysts: a review, RSC Adv. 5 (2015) 14610–14630.

[2] A. Fujishima, K. Honda, Electrochemical photolysis of water at a semiconductor electrode, Nature 238 (1972) 37–38.

[3] A. Kudo, Y. Miseki, Heterogeneous photocatalyst materials for water splitting, Chem. Soc. Rev. 38 (2009) 253–278.

[4] V.L. Prasanna, R. Vijayaraghavan, Insight into the mechanism of antibacterial ac-tivity of ZnO: surface defects mediated reactive oxygen species even in the dark, Langmuir 31 (2015) 9155–9162.

[5] S. Rehman, R. Ullah, A.M. Butt, N.D. Gohar, Strategies of making TiO$_2$ and ZnO visible light active, J. Hazard. Mater. 170 (2009) 560–569.

[6] R. Asahi, T. Morikawa, T. Ohwaki, K. Aoki, Y. Taga, Visible-light photocatalysis in nitrogen-doped titanium oxides, Science 293 (2001) 269–271.

[7] H.J. Zhang, G.H. Chen, D.W. Bahnemann, Photoelectrocatalytic materials for en-vironmental applications, J. Mater. Chem. 19 (2009) 5089–5121.

[8] F. Dong, H.Q. Wang, Z.B.J. Wu, One-step green synthetic approach for mesoporous C-doped titanium dioxide with efficient visible light photocatalytic activity, Phys. Chem. C 113 (2009) 16717–16723.

[9] D. Dvoranová, V. Brezová, M. Mazúr, M.A. Malati, Investigations of metal-doped titanium dioxide photocatalysts, Appl. Catal. B: Environ. 37 (2002) 91–105.

[10] F. Dong, S. Guo, H. Wang, X. Li, Z. Wu, Enhancement of the visible light photo-catalytic activity of C-doped TiO$_2$ nanomaterials prepared by a green synthetic

A. Šutka et al.
Journal of Environmental Chemical Engineering 6 (2018) 2606–2615

approach, J. Phys. Chem. C 115 (2011) 13285–13292.

[11] S. Tokunaga, H. Kato, A. Kudo, Selective preparation of monoclinic and tetragonal BiVO$_4$ with scheelite structure and their photocatalytic properties, Chem. Mater. 13 (2001) 4624–4628.

[12] W. Morales, M. Cason, O. Aina, N.R. de Tacconi, K. Rajeshwar, Combustion synthesis and characterization of nanocrystalline WO$_3$, J. Am. Chem. Soc. 130 (2008) 6318–6319.

[13] B. Ahmmad, K. Leonard, Md.S. Islam, J. Kurawaki, M. Muruganandham, T. Ohkubo, Y. Kuroda, Green synthesis of mesoporous hematite (α-Fe$_2$O$_3$) nanoparticles and their photocatalytic activity, Adv. Powder Technol. 24 (2013) 160–167.

[14] C. Yu, G. Li, S. Kumar, K. Yang, R. Jin, Phase transformation synthesis of novel Ag$_2$O/Ag$_2$CO$_3$ heterostructures with high visible light efficiency in photocatalytic degradation of pollutants, Adv. Mater. 26 (26) (2014) 892–898.

[15] L. Huang, F. Peng, H. Yu, H. Wang, Preparation of cuprous oxides with different sizes and their behaviors of adsorption, visible-light driven photocatalysis and photocorrosion, Solid State Sci. 11 (2009) 129–138.

[16] H. Wang, L. Zhang, Z. Chen, J. Hu, S. Li, Z. Wang, J. Liu, X. Wang, Semiconductor heterojunction photocatalysts: design, construction, and photocatalytic performances, Chem. Soc. Rev. 43 (2014) 5234–5244.

[17] H. Li, Y. Zhou, W. Tu, J. Ye, Z. Zou, State-of-the-art progress in diverse hetero-structured photocatalysts toward promoting photocatalytic performance, Adv. Funct. Mater. 25 (2015) 998–1013.

[18] P. Zhou, J. Yu, M. Jaroniec, All-solid-state Z-scheme photocatalytic systems, Adv. Mater. 26 (2014) 4920–4935.

[19] H. Li, W. Tu, Y. Zhou, Z. Zou, Z-scheme photocatalytic systems for promoting photocatalytic performance: recent progress and future challenges, Adv. Sci. 3 (2016) 1500389.

[20] L.J. Zhang, S. Li, B.K. Liu, D.J. Wang, T.F. Xie, Highly efficient CdS/WO$_3$ photocatalysts: Z-scheme photocatalytic mechanism for their enhanced photocatalytic H$_2$ evolution under visible light, ACS Catal. 4 (2014) 3724–3729.

[21] W.K. Jo, T. Adinaveen, J.J. Vijaya, N.C.S. Selvam, Synthesis of MoS$_2$ nanosheet supported Z-scheme TiO$_2$/g-C$_3$N$_4$ photocatalysts for the enhanced photocatalytic degradation of organic water pollutants, RSC Adv. 6 (2016) 10487–10497.

[22] J.-C. Wang, H. -Ch. Yao, Z.-Y. Fan, L. Zhang, J.-S. Wang, S.-Q. Zang, Z.-J. Li, Indirect Z-scheme BiOI/g-C3N4 photocatalysts with enhanced photoreduction CO2 activity under visible light irradiation, ACS Appl. Mater. Interfaces 8 (2016) 3765–3775.

[23] K.J. McDonald, K.-S. Choi, Synthesis and photoelectrochemical properties of Fe$_2$O$_3$/ZnFe$_2$O$_4$ composite photoanodes for use in solar water oxidation, Chem. Mater. 23 (2011) 4863–4869.

[24] L. Li, P.A. Salvador, G.S. Rohrer, Photocatalysts with internal electric fields, Nanoscale 6 (2014) 24–42.

[25] P.G. Vekilov, The two-step mechanism of nucleation of crystals in solution, Nanoscale 2 (2010) 2346–2357.

[26] J. van Embden, A.S.R. Chesman, J.J. Jasieniak, The heat-up synthesis of colloidal nanocrystals, Chem. Mater. 27 (2015) 2246–2285.

[27] J.P. Jolivet, C. Chaneac, E. Tronc, Iron oxide chemistry. From molecular clusters to extended solid networks, Chem. Commun. 10 (2004) 481–483.

[28] D.M. Sherman, Electronic spectra of Fe^{3+} oxides and oxide hydroxides in the near IR to near UV, Am. Miner. 70 (1985) 1262–1269.

[29] A.B. Murphy, Band-gap determination from diffuse reflectance measurements of semiconductor films, and application to photoelectrochemical water-splitting, Sol. Energy Mat. Sol. C 91 (2007) 1326–1337.

[30] K. Sivula, F. Le Formal, M. Grätzel, Solar water splitting: progress using hematite ((αFe$_2$O$_3$) photoelectrodes, ChemSusChem 4 (2011) 432–449.

[31] C.P. Jijil, M. Lokanathan, S. Chithiravel, C. Nayak, D. Bhattacharyya, S.N. Jha, P.D. Babu, B. Kakade, R. Nandini Devi, N doping in oxygen deficient Ca$_2$Fe$_2$O$_5$: a strategy for efficient oxygen reduction oxide catalysts, ACS Appl. Mater. Interfaces 8 (2016) 34387–34395.

[32] S. Zhang, J. Li, H. Niu, W. Xu, J. Xu, W. Hu, X. Wang, Visible-light photocatalytic degradation of methylene blue using SnO$_2$/a-Fe$_2$O$_3$ hierarchical nanoheterostructures, ChemPlusChem 78 (2013) 192–199.

[33] Y. Wang, Y. Wang, Y. Gao, Photocatalytic H$_2$ evolution from water in the presence of carbon dioxide over NiO/Ca$_2$Fe$_2$O$_5$, React. Kinet. Mech. Cat. 99 (2010) 485–491.

[34] H. Li, H. Yu, X. Quan, S. Chen, Y. Zhang, Uncovering the key role of the Fermi level of the electron mediator in a Z-scheme photocatalyst by detecting the charge transfer process of WO$_3$-metal-gC$_3$N$_4$ (metal Cu, Ag Au), ACS Appl. Mater. Interfaces 8 (2016) 2111–2119.

[35] H. Tada, T. Mitsui, T. Kiyonaga, T. Akita, K. Tanaka, All-solid-state Z-scheme in CdS–Au–TiO$_2$ three-component nanojunction system, Nat. Mat. 5 (2016) 782–786.

[36] N. Srinivasan, E. Sakai, M. Miyauchi, Balanced excitation between two semiconductors in bulk heterojunction Z-scheme system for overall water splitting, ACS Catal. 6 (2016) 2197–2200.

[37] J.-C. Wang, L. Zhang, W.-X. Fang, J. Ren, Y.-Y. Li, H.-C. Yao, J.-S. Wang, Z.-J. Li, Enhanced photoreduction CO$_2$ activity over direct Z-scheme α-Fe$_2$O$_3$/Cu$_2$O heterostructures under visible light irradiation, ACS Appl. Mater. Interfaces 7 (2015) 8631–8639.

[38] E. Asenath-Smith, I.N. Lokuhewa, S.T. Misture, D.D. Edwards, p-Type thermoelectric properties of the oxygen-deficient perovskite Ca$_2$Fe$_2$O$_5$ in the brownmillerite structure, J. Solid State Chem. 183 (2010) 1670–1677.

[39] A. Hellman, R.G.S. Pala, First-principles study of photoinduced water-splitting on Fe$_2$O$_3$, J. Phys. Chem. C 115 (2011) 12901–12907.

[40] R.L. Spray, K.-S. Choi, Photoactivity of transparent nanocrystalline Fe$_2$O$_3$ electrodes prepared via anodic electrodeposition, Chem. Mater. 21 (2009) 3701–3709.

[41] S. Dhankhar, K. Gupta, G. Bhalerao, N. Shukla, M. Chandran, B. Francis, B. Tiwari, K. Baskara, S. Singh, Anomalous room temperature magnetoresistance in brownmillerite Ca$_2$Fe$_2$O$_5$, RSC Adv. 5 (2015) 92549–92553.

[42] S.D. Tilley, M. Cornuz, K. Sivula, M. Grätzel, Light-induced water splitting with hematite: improved nanostructure and iridium oxide catalysis, Angew. Chem. Int. Ed. 122 (2010) 6549–6552.

[43] Y.-K. Hsu, Y.-C. Chen, Y.-G. Lin, Novel ZnO/Fe$_2$O$_3$ core–shell nanowires for photoelectrochemical water splitting, ACS Appl. Mater. Interfaces 7 (2015) 14157–14162.

[44] M.G. Ahmed, T.A. Kandiel, A.Y. Ahmed, I. Kretschmer, F. Rashwan, D. Bahnemann, Enhanced photoelectrochemical water oxidation on nanostructured hematite photoanodes via p-CaFe$_2$O$_4$/n-Fe$_2$O$_3$ heterojunction formation, J. Phys. Chem. C 119 (2015) 5864–5871.

[45] Y. Yang, Z. Cao, Y. Jiang, L. Liu, Y. Sun, Photoinduced structural transformation of SrFeO$_3$ and Ca$_2$Fe$_2$O$_5$ during photodegradation of methyl orange, Mater. Sci. Eng. B 132 (2006) 311–314.

2615